SCIENCE CHINA
Technological Sciences

•Article•

December 2020 Vol.63 No.12: 2541–2552
https://doi.org/10.1007/s11431-020-1676-7

Modeling and experiments of a nano-positioning and high frequency scanning piezoelectric platform based on function module actuator

DENG Jie, LIU YingXiang*, ZHANG ShiJing & LIU JunKao

School of Mechatronics and Engineering, Harbin Institute of Technology, Harbin 150001, China

Received March 22, 2020; accepted June 12, 2020; published online August 17, 2020

A piezoelectric platform using function module actuator is presented to achieve nano-positioning and high frequency scanning in large working range. A function module actuator is designed to produce a pair of orthogonal bending deformations and a longitudinal deformation through partition exciting. The bending deformations are used to actuate the planar motion, while the longitudinal deformation is utilized to dynamically adjust the driving force and broaden the scanning frequency. The dynamic model of the platform system is developed. The open-loop performances of a prototype are first tested: a scan frequency of 308 Hz in a scanning range of 3.368 μm×3.396 μm is measured in direct actuation mode, and the displacement resolution is measured to be 16 nm; maximum speed is measured to be 3.38 mm s^{-1} in the inertial actuation mode. Furthermore, the closed-loop experiments are carried out and a switching strategy is proposed to obtain the switching of the inertial and direct actuation modes automatically; the platform achieves the scanning with frequency of 300 Hz at the set position.

piezoelectric actuator, function modules, nano-positioning platform, large working range, high frequency scanning

Citation: Deng J, Liu Y X, Zhang S J, et al. Modeling and experiments of a nano-positioning and high frequency scanning piezoelectric platform based on function module actuator. Sci China Tech Sci, 2020, 63: 2541–2552, https://doi.org/10.1007/s11431-020-1676-7

1 Introduction

Piezoelectric nano-positioning platforms, which generally refer to piezoelectric actuated mechanisms with planar output capability, have been widely applied in ultraprecision fields such as ultraprecision manufacturing [1,2], optical imaging [3,4], and biomedicine [5,6]. The nano-positioning platforms should have characteristics of nanometer resolution, large working range and good mechanical dynamic to satisfy the requirements of these fields. Piezoelectric actuator is a promising candidate for the actuation unit of the platforms, as its merits of fast response, easy realization of nanometer resolution and flexible structure [7–11]. The tube-shaped piezoelectric actuator (TPA) is widely used to achieve planar motion with nanometer resolution, the output platform is driven to realize planar motion through its bending motions [12]; the piezoelectric tube driving platform is commercial for many years because of the simple structure. However, the resonance frequency of TPA is relatively low due to the large length-to-diameter ratio; the dynamic characteristics are not good enough, thus, limiting the mechanical bandwidth [13].

The flexure-hinge-guided platform is another way to achieve the planar nano-positioning with relatively high mechanical resonance frequency, a wide mechanical bandwidth can be achieved; the output platform and piezoelectric actuators are connected by flexible-hinges, the displacement of the actuator is amplified by flexure-hinges and outputted through the output platform, in which the PZT stack actuator (PSA) is employed [14]. For example, Yong et al. [15] pre-

*Corresponding author (email: liuyingxiang868@hit.edu.cn)

sented a nano-positioner with a wide mechanical bandwidth, the first mechanical resonant frequency along axis X was improved to 8.8 kHz, high displacement resolution outputs were successfully achieved. Watanabe and Ando [16] proposed a high-speed XYZ-nano-positioner with first resonance frequencies of 100 kHz for axis Z and 2.3 kHz for axes X and Y, a good mechanical dynamic was obtained, the high-speed imaging of 3.5 s frame^{-1} was achieved. The good mechanical dynamics and nanometer resolution allow the flexure-hinge-guided platforms to be applied in high-accuracy nano-positioning devices, and are employed in several commercial equipment. However, the hysteresis behavior exists in the piezoelectric actuators, especially the PSA, which is researched by some researchers to solve the problem [17–21]. Moreover, the working range of the platform is limited to hundreds of square micrometers, because the stroke of PSA is only approximately 0.1% of the total length; then amplification designs are utilized to amplify output displacements by some scholars [22,23], the working range is extended, but the configuration of the platform is complex, which is hard to manufacture.

The stepping type piezoelectric platform can alleviate the problem of small working range, a large working range can be obtained by the stepping movements of the output platform [24–28]. Chen et al. [29] developed a stepping actuator, a large working range was achieved. Liu et al. [30] proposed a piezoelectric stepping platform using longitudinal-bending hybrid actuators, large working range was obtained, the displacement resolutions in the two directions were 0.1 and 0.2 μm, respectively. As a result, a large working range is obtained through the accumulation of the small steps for the stepping type piezoelectric platform. The inertial actuation mode is a typical actuation method for the stepping platform systems because of the simple exciting signal, some platforms adopting inertial actuation mode are commercially available, such as the MechOnics AG, New Scale Technology, etc. However, the resolution of the inertial platform is not high enough, which limits its application.

High precision positioning and large working range can be achieved by combining the direct and inertial actuation modes, the platform obtains nanometer resolution and large working range by the direct and inertial actuation modes, respectively [31–33]. In this study, a piezoelectric nano-positioning platform using function module actuator is presented, in which the direct and inertial actuation modes are used together to achieve the nano-positioning and high frequency scanning in large working range. In Section 2, the structure and operating principle are presented. In Section 3, modeling of the platform system is presented. In Section 4, experiments are carried out, the outputs in the direct and inertial actuation modes are investigated. Section 5 is the conclusion.

2 Platform structure and motion planning

The piezoelectric platform is consisted of an output platform, a set of rail slider system, a piezoelectric function module actuator and a base (Figure 1(a)). The slider system is composed of two groups of orthogonal guiding systems, in which one group consists of two guide rails and four sliders, the two groups are responsible for the guidance, and a connecting rack is designed to connect them. The function module actuator is mainly composed of five groups of PZT function modules and they are connected together through a connecting bolt. An insulating sleeve is used to separate the PZT function modules and the connecting bolt (Figure 1(b)). Arrangement of the function modules can be seen in

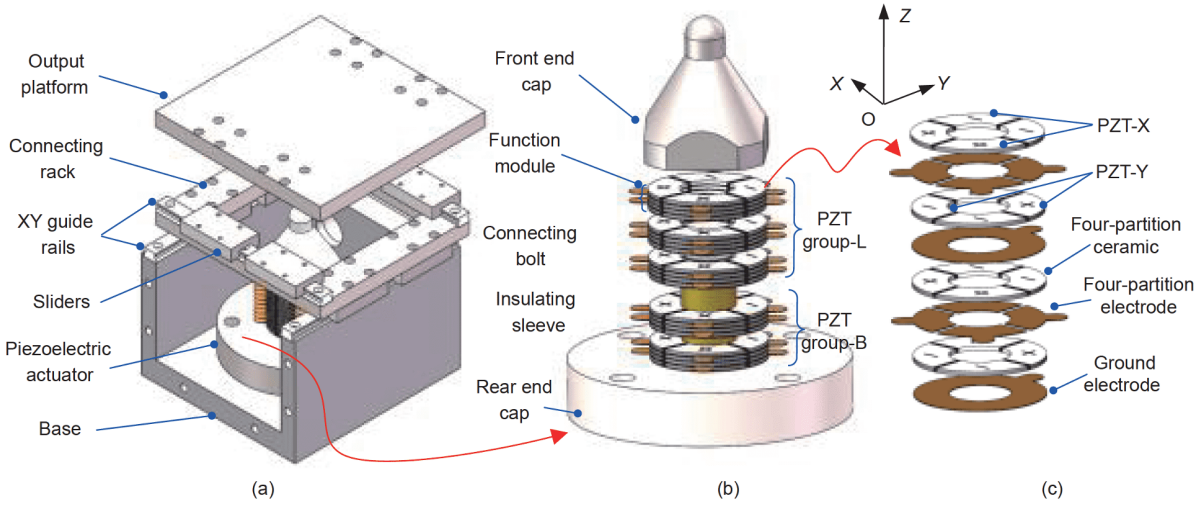

Figure 1 (Color online) Schematic diagram of the proposed piezoelectric platform system. (a) Configuration of the platform system; (b) three dimensional graph of the function module actuator; (c) arrangement of the piezoelectric function module.

Figure 1(c), a group of PZT function module is consisted of four pieces of four-partition PZT rings, the four-partition electrode and the ground electrode are arranged alternately between two adjacent ceramic pieces, the voltage excitation signals are applied to the ceramic rings through them. This arrangement can ensure that all ceramic rings have the same deformation by operating in the d_{33} mode. The four partitions are divided into two groups, the group whose diagonal line is along axis X is named as PZT-X, whereas another group is named as PZT-Y. The function module can bend along axis X as the same voltages are applied to PZT-X through the four-partition electrodes, in which one partition extends and another partition shortens; and the bending along axis Y can also be obtained by the same exciting method. In another hand, the function module can extend or shorten longitudinally along axis Z when the four partitions are excited separately and extend or shorten at the same time. As a result, the function module can bend along axes X and Y, or vibrate along axis Z. Each function module can complete different actuation actions independently, which allows flexible combination of the function modules to achieve multiple actuation modes.

The platform is designed to realize nano-positioning and high frequency scanning in large working range, the method combining the direct actuation mode and the inertial actuation mode is adopted, and five groups of function modules are selected for realizing the combination actuation modes, which are arranged as follows: the three groups of function modules near the front end cap are employed for the longitudinal deformation of the actuator, which are used to adjust the normal pressure, thus to control the driving force, named as PZT group-L; while the remaining two groups are employed to produce bending motions, which can be utilized to drive the output platform, named as PZT group-B.

For the direct actuation mode, the operating steps are presented in Figure 2(a), which can be achieved through combining the longitudinal and bending deformations of the function modules, the corresponding exciting signals and response operations are shown in Figure 3(a): in step (1), exciting voltage signals applied to the PZT group-L are set as positive value, the actuator extends in the vertical direction and clamps the output platform; in step (2), voltage signals applied to the PZT-X or PZT-Y of the PZT group-B are set as positive value, the motions along axis X or axis Y in plane can be achieved by static friction force. The deformation of the longitudinal function module is adopted to improve the clamping force in the operating process and enhance the contact stiffness between the driving tip and output platform, thus to improve the dynamic characteristic of the platform and broaden the scanning bandwidth.

The inertial actuation mode is selected for the stepping actuation as the simple exciting signal and high output speed, which is based on the stick-slip mechanism. Bending and longitudinal deformations of the function modules are combined to improve the classical inertial actuation mode, the former one is used to actuate the output platform, the latter one is utilized to enhance the friction force in the sticking process and reduce the friction force in the slipping process, which is helpful to alleviate the inherent rollback problem existing in the classical inertial actuator and increase the output speed. There are four operating steps in the operating process (Figure 2(b)), the corresponding exciting signals and response operations are presented in Figure 3(b). In details, the operating steps for the motion along axis X (positive direction) are as follows.

Step (1): in time interval t_1, signals applied to the PZT-X decreases rapidly to $-V_{max}$, the actuator bends fast along axis X (negative direction) and the driving tip moves to the negative direction of axis X, the platform can keep still due to the inertial in theory.

Step (2): in time interval t_2, voltage signals applied to the PZT group-L are set as positive value, the actuator extends and its driving tip clamps the output platform.

Step (3): in time interval t_3, signals applied to the PZT-X

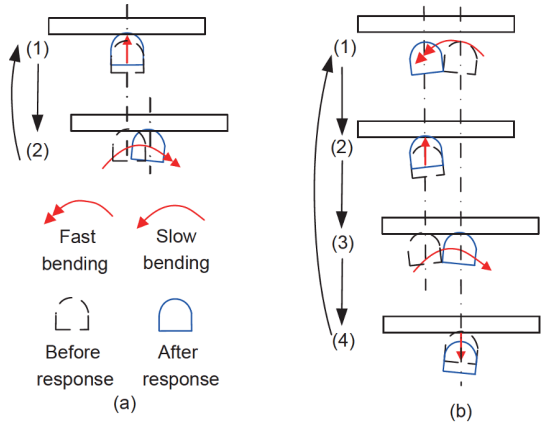

Figure 2 (Color online) The operating steps. (a) Operating steps of the direct actuation mode; (b) operating steps of the inertial actuation mode.

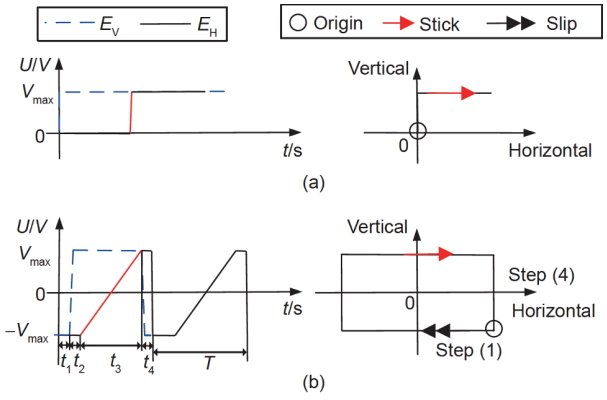

Figure 3 (Color online) The exciting signals and operations for the actuation modes. (a) Signals and operations for direct actuation mode; (b) signals and operations for inertial actuation mode.

increases slowly from $-V_{max}$ to V_{max}, the actuator bends slowly along axis X (positive direction) and the driving tip moves to the positive direction of axis X, the output platform follows the driving tip through the static friction force, and it is moved for one step.

Step (4): in time interval t_4, voltage signals applied to the PZT group-L are set as negative value, the actuator shortens and the driving tip separates from the output platform.

Step (5): repeats (1)–(4).

Thus, the stepping motion along axis X (positive direction) can be achieved by repeating the above steps, and the motion in large working range can be obtained.

3 Modeling of the platform

The dynamic model for the piezoelectric platform system is developed, mainly composed of two steps: firstly, dynamic modeling for the PZT function module actuator, secondly, contact modeling for the actuator and the output platform.

3.1 Model of the piezoelectric function module actuator

The actuator performs bending and longitudinal deformations in the operating process, which are generated by exciting PZT group-B and PZT group-L, respectively. The bending deformations along axes X and Y, and the longitudinal deformation along axis Z of the actuator are independent of each other, thus, the models of them are established separately. The structure of the piezoelectric actuator is shown in Figure 4.

3.1.1 *Modeling of the bending deformation*

The bending deformation of the actuator is shown in Figure 4(c), which can be modeled based on the Timoshenko beam theory. The bending deformation along axis X is developed firstly. Given by

$$\frac{\partial w}{\partial z}=\theta=\psi+\gamma, \tag{1}$$

$$\gamma=\frac{P}{kGA}, \tag{2}$$

where ψ is the rotation and γ is the shear of the cross section. w is the bending displacement, k is the shear coefficient for the bending deformation [34]. The moment for the deformation is given by

$$M=EI\frac{\partial\psi}{\partial z}. \tag{3}$$

Force analysis is performed in the differential element, given by

$$\begin{cases}\rho_e A\dfrac{\partial^2 w}{\partial t^2}\mathrm{d}z=P+\dfrac{\partial P}{\partial z}\mathrm{d}z-P,\\ \rho_e I\dfrac{\partial^2\psi}{\partial t^2}\mathrm{d}z=\dfrac{\partial M}{\partial z}\mathrm{d}z+M+P\mathrm{d}z-M,\end{cases} \tag{4}$$

where ρ_e is the area density and A is the cross section area of

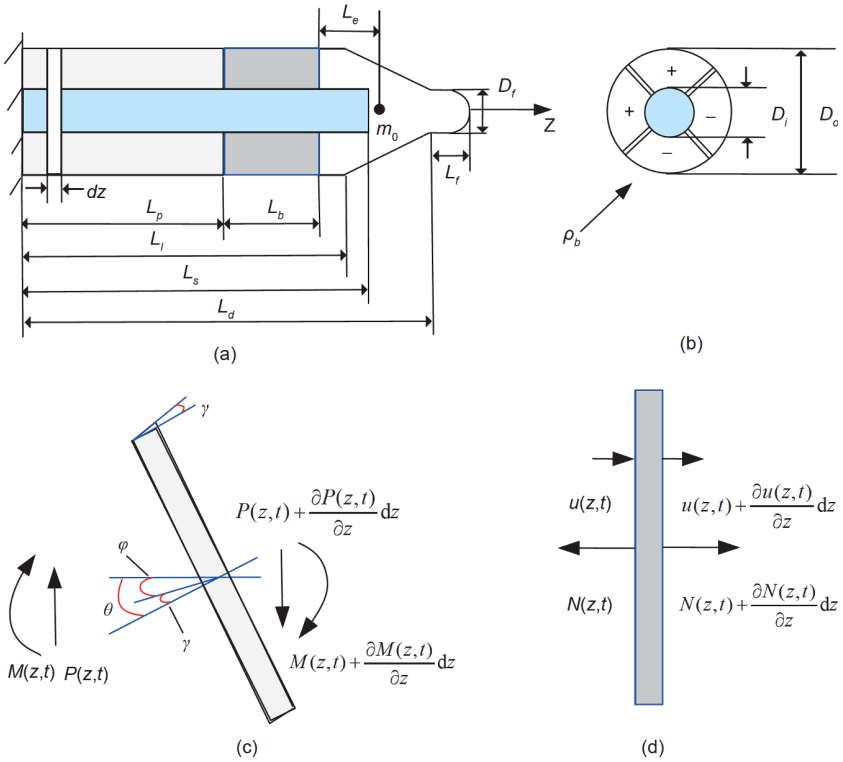

Figure 4 (Color online) Dynamic modeling for PZT function module actuator. (a) Structure of the actuator; (b) cross section of the PZT part; (c) the bending deformation in differential element; (d) the longitudinal deformation in differential element.

the differential element, respectively.

It can be obtained from eqs. (1) to (4):

$$EI\frac{\partial^4 w}{\partial z^4}+\rho_e A\frac{\partial^2 w}{\partial t^2}-\rho_e I\left(1+\frac{E}{kG}\right)\frac{\partial^4 w}{\partial t^2\partial z^2}+\frac{\rho_e{}^2 I}{kG}\frac{\partial^4 w}{\partial t^4}=0. \tag{5}$$

Eq. (5) can be solved by Galerkin procedure and the bending displacement $w(z, t)$ can be written as

$$w(z,t)=\sum_{i=1}^{n}\varphi_i(z)r_i(t), \tag{6}$$

where $\varphi_i(z)$ and $r_i(t)$ are the mode shapes for the bending motion and the modal mechanical response for the system, respectively, written as

$$\varphi_i(z)=a_i\sin\lambda_i z+b_i\cos\lambda_i z+c_i\sinh\lambda_i z+d_i\cosh\lambda_i z, \tag{7}$$

$$r_i(t)=e\sin\omega_i t+f\cos\omega_i t, \tag{8}$$

where a to f are constants determined by the structure of the actuator, ω_i is the natural frequency which determines the coefficient λ_i.

The front cap end and PZT group-L can be regarded as a mass load of m_0 with equivalent distance of L_e. The mode shape $\varphi_i(z)$ is determined and calculated by the boundary conditions, the mode shape $\varphi_i(z)$ and the natural frequency ω_i can be obtained. The first mode shape $\varphi_1(z)$ can describe the dynamic characteristics accurately because it operates in the nonresonant mode [35], therefore, i is selected as 1 in this work.

3.1.2 *Modeling of the longitudinal deformation*

The longitudinal deformation can be seen in Figure 4(d). And differential equation in the differential element is given by

$$\rho_e A\frac{\partial^2 u}{\partial t^2}\mathrm{d}z=N+\frac{\partial N}{\partial z}\mathrm{d}z-N. \tag{9}$$

The axial force N is

$$N=EA\varepsilon=EA\frac{\partial u}{\partial z}, \tag{10}$$

where ε is the strain in the differential element.

Eliminating N from the above two equations, given by

$$\frac{\partial^2 u}{\partial t^2}=\frac{E}{\rho_e}\frac{\partial^2 u}{\partial z^2}. \tag{11}$$

Eq. (11) can be solved by separation variable method, and the longitudinal displacement $u(z, t)$ is

$$u(z,t)=\sum_{i=1}^{n}\phi_i(z)q_i(t), \tag{12}$$

where ϕ_i is the mode shapes and q_i is the modal mechanical response, given by

$$\phi_i(z)=a_{1i}\sin\lambda_{1i}z+b_{1i}\cos\lambda_{1i}z, \tag{13}$$

$$q_i(t)=e_{1i}\sin\omega_{1i}t+f_{1i}\cos\omega_{1i}t, \tag{14}$$

where a_{1i}, b_{1i}, e_{1i} and f_{1i} are constant coefficients, ω_{1i} is the longitudinal natural frequency, λ_{1i} is determined by ω_{1i}, as

$$\omega_{1i}=\lambda_{1i}\sqrt{\frac{E}{\rho_e}}. \tag{15}$$

Similarly, they can be calculated by the boundary conditions.

3.1.3 *System governing equations*

The Lagrange's equations is adopted to obtain the modal mechanical responses of the deformations, in which the solution processes are the same. The equation of the bending deformation is given by

$$\frac{\partial}{\partial t}\left(\frac{\partial L}{\partial \dot{r}}\right)-\left(\frac{\partial L}{\partial r}\right)=\frac{\delta W}{\delta r}, \tag{16}$$

where L and W are the Lagrange function and virtual work of the system. Lagrange function is written as

$$L=T-U, \tag{17}$$

where T and U are the kinetic energy and potential energy of the system.

The following state equations are obtained by using the Lagrange's equation:

$$\begin{cases}\ddot{r}(t)+\eta\dot{r}(t)+\upsilon r(t)-\kappa=\zeta V(t),\\ \ddot{q}(t)+\eta_1\dot{q}(t)+\upsilon_1 q(t)-\kappa_1=\zeta_1 V(t).\end{cases} \tag{18}$$

As a result, the transfer functions for bending and longitudinal displacements of the driving tip and the applied exciting signals can be obtained by Laplace transform

$$G(s)=\frac{w(s)}{V(s)}=\frac{\zeta\left(\varphi(L_p)+(L_d+L_f-L_p)\frac{\partial\varphi(z)}{\partial z}\Big|_{z=L_p}\right)}{s^2+\eta s+\upsilon}, \tag{19}$$

$$H(s)=\frac{u(s)}{V(s)}=\frac{\zeta_1\phi(L_b)}{s^2+\eta_1 s+\upsilon_1}. \tag{20}$$

3.2 Contact model

The classical tangential contact theory [36] for an elastic sphere pressed into an elastic half space with partial slip is adopted in this study. The driving tip of the actuator and the output platform are considered as a sphere and a smooth rigid surface, as shown in Figure 5. A normal static pressure F_N is applied and the driving tip press on the output platform, the tangential inertial force F_X is produced by the relative slippage, the motion of the output platform is formed by the tangential friction force generated by friction between the two surfaces.

$$a^2=Rd, \tag{21}$$

where R is the sphere's radius, d is the indentation depth and a is the contact radius,

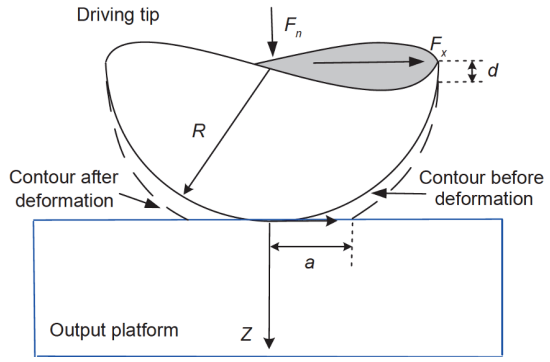

Figure 5 (Color online) Tangential contact of a sphere.

The equivalent Young's modulus is defined as

$$\frac{1}{E}=\frac{1-v_1^2}{E_1}+\frac{1-v_2^2}{E_2}, \tag{22}$$

where E and v are the Young's modulus and the Poisson's ratio.

The surface of the output platform is assumed to be consisted of some micro-convex bodies, the origin of axis Z is defined as the average surface height of all micro-convex bodies, h_0 is the height of the smooth surface. The height distribution of the micro-convex bodies conforms to Gaussian distribution, given by

$$\Phi(z)=\left(\frac{1}{2\pi l^2}\right)^{\frac{1}{2}}e^{\frac{-z^2}{2l^2}}, \tag{23}$$

where l is the root mean square of the height distribution, which is the roughness of the contact area.

According to the GM model, the relationship between the height h_0 and the preload F_0 can be calculated by the following equation:

$$F_0=\int_{h_0}^{\infty}N_0\Phi(z)\frac{4}{3}ER^{\frac{1}{2}}(z-h_0)^{\frac{3}{2}}\mathrm{d}z, \tag{24}$$

where N_0 is the number of the micro-convex body, h_0 can be obtained by the above equation when the preload force F_0 is known.

The normal total contact force is F_d, which can be calculated by

$$F_d=\begin{cases}0 & z<h_0-V,\\ \displaystyle\int_{h_0-v(t)}^{\infty}N_0\Phi(z)2ER^{\frac{1}{2}}(z-h_0)^{\frac{1}{2}}(z+u(t)-h_0)dz & z\geq h_0-V,\end{cases} \tag{25}$$

where $u(t)$ and V are the longitudinal response displacement of the driving tip and the amplitude, they can be obtained by the dynamic model of the piezoelectric actuator.

The tangential friction force f_X can be calculated by the relationship between the sliding friction force and the tangential inertial force F_X, given by

$$f_X=\begin{cases}0, & \mu F_d\leq 0,\\ \mu F_d, & \mu F_d\leq F_x,\\ \sigma(v_x-v_s), & \mu F_d>F_x,\end{cases} \tag{26}$$

$$F_X=m\ddot{w}(t), \tag{27}$$

where μ is the sliding friction coefficient and σ is the viscous friction coefficient, respectively. v_x is horizontal bending speed at the driving tip of the actuator, v_s is the response speed of the output platform, m is the mass of the runner part, including the output platform and the sliders, $w(t)$ is the bending displacement of the driving tip excited by the applied voltage signals.

The tangential friction force drives the output platform to move in the horizontal plane, the output displacement can be calculated by

$$s(t)=\iint\frac{f_X}{m}\mathrm{d}t^2. \tag{28}$$

Therefore, the dynamic model of the piezoelectric platform system can be achieved, which can be simulated by Simulink.

The material of the PZT are selected as PZT-4, the mass density is 7600 kg m^{-3}. The material of the front end cap is aluminum alloy, the mass density is 2810 kg m^{-3}, Young's modulus of and Poisson ratio are 70 GPa and 0.3. The end cap and connecting bolt are 45# steel, the mass density is 7800 kg m^{-3}, Young's modulus and Poisson ratio are 206 GPa and 0.3. The dimension and materials parameters of the system are presented in Tables 1 and 2.

4 Platform characteristics experiments

The experiment set-up was established to verify the feasibility of the operating principle and the dynamic model (see Figure 6). The piezoelectric ceramics are provided by the

Table 1 Dimension parameters of the actuator

Structure dimensions	Values (mm)	Structure dimensions	Values (mm)
L_p	14.4	L_f	10
L_b	9.6	D_i	14
L_l	30	D_o	30
L_s	40	D_f	10
L_d	50		

Table 2 Parameters used in the contact model

Parameter	Value	Parameter	Value
Number of the convex body (N_0)	655.4×7.85 [37]	Poisson's ratio of the output platform (v_2)	0.25
Height of the smooth surface (h_0)	0.3 μm	Sliding friction coefficient (μ)	0.15
Roughness (R_a)	0.32 μm	Viscous friction coefficient (σ) [37]	$\sqrt{10^5}$ N·s/m
Radius of the micro-convex body (R)	3.2 μm	Mass along axis X (m_X)	0.486 kg
Young's modulus of the output platform (E_2)	195 GPa	Mass along axis Y (m_Y)	0.598 kg

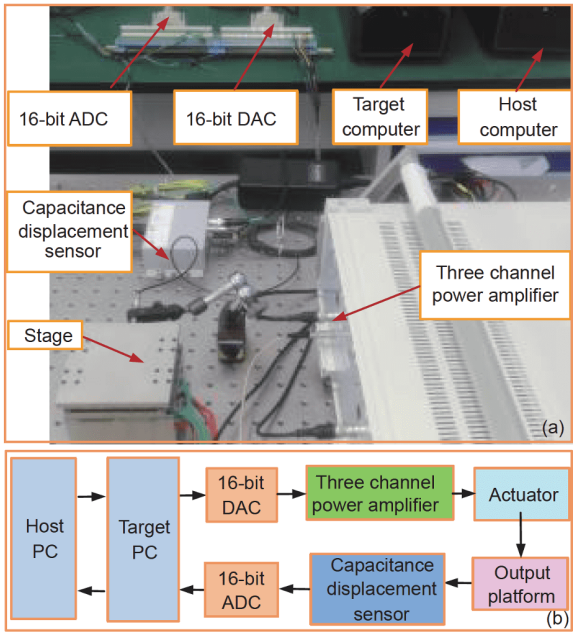

Figure 6 (Color online) Experiment system. (a) Experiment set-up; (b) control system.

46th Institute of CECT. A capacitance displacement sensor (PI D-E20.050, Germany) was adopted to measure the response displacement, the dynamic measuring resolution and measurement range were 1.5 nm and 50 μm, the bandwidth was 1.24 kHz. The 16-bit DACs and ADCs (Advantech, China) were adopted to generate and capture signals of the system.

4.1 Model verification

Experiments in the direct and inertial actuation modes are carried out to evaluate the efficiency of the model. For easy comparison, only motion along axis X is presented due to the same operation along axes X and Y.

4.1.1 Direct actuation mode

Results in Figure 7 show the comparisons between the simulation and the experimental results in the direct actuation mode under sinusoidal signals, the frequencies are 0.1, 1 and 10 Hz, respectively, in which the voltage of the signal is 600 $V_{p\text{-}p}$. The result demonstrates that the model is effective. However, there is a big difference between the simulation and experimental results at 100 Hz, this is because the friction coefficients vary with frequency, the used values are constants in the contact model for simplicity, thus, the higher the frequency, the greater the difference between them, the piecewise sliding and viscous friction coefficients in different frequency bands can be adopted to obtain a more accurate model in the further study. As a result, the proposed model can agree well with the experiment in low frequency band.

4.1.2 Inertial actuation mode

The exciting signals are that in Figure 2(b), the voltage and frequency are 600 $V_{p\text{-}p}$ Hz and 1 Hz. The results are presented in Figure 8(a), the displacement in one cycle is similar with the signal applied to PZT-X and stepping motions are generated. It can be seen that the experimental results coincide with the simulation results. The step distances along axis X obtained by experiment and simulation are 3.17 and 4.02 μm, respectively. The measured step distance is smaller than the simulation one because rollbacks occur at steps (1), (2) and (4), respectively. The enlargement of one cycle is shown in Figure 8(b). The reasons for the rollback phenomenon are explained as follows: in step (1), the longitudinal deformation of function modules cannot make the complete separation between the output platform and driving tip, the rollback is about 0.36 μm; in step (2), voltage applied to the PZT-X is negative, the driving tip of the actuator moves to the negative direction, the output platform also moves to the negative direction when the PZT group-L extends because the connection stiffness between the output platform and the sliders is not high enough, and the rollback is 0.41 μm; in step (4), the output platform moves backward when the PZT group-L shortens due to the same reason, the rollback is 0.09 μm. Thus, the efficiency of the model is verified, the differences are mainly caused by the manufacturing and assembly errors.

Therefore, the efficiency of the proposed model is verified in low frequency band in both the direct and inertial actuation modes. The proposed model can be used for structural design of the platform composed of function modules. Besides, it can be utilized to design the exciting scheme for platforms operating in multiple actuation modes.

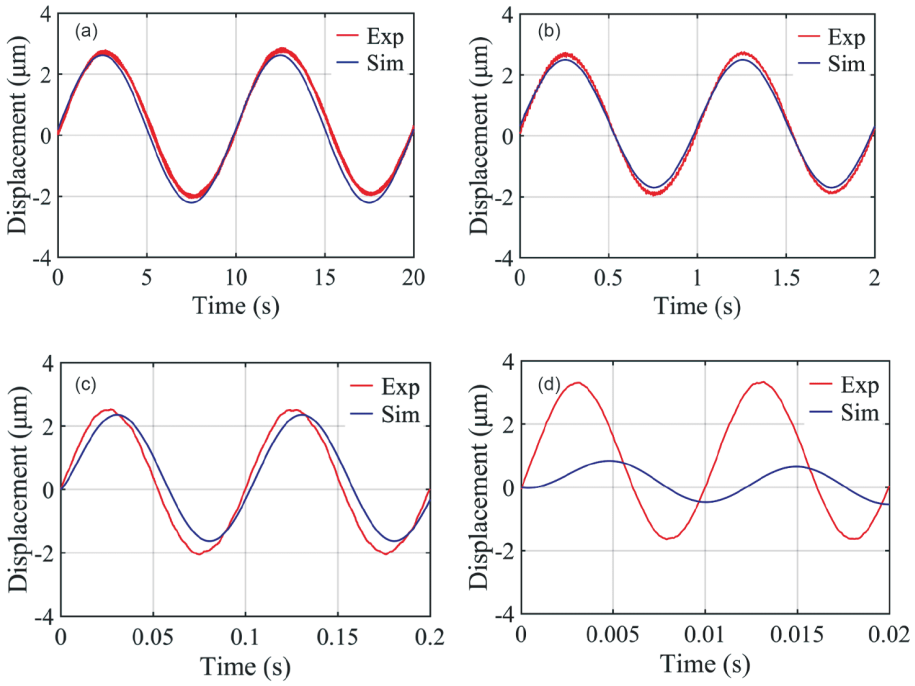

Figure 7 (Color online) The simulation and the experimental results in the direct actuation mode under sinusoidal signals. (a) 0.1 Hz; (b) 1 Hz; (c) 10 Hz; (d) 100 Hz.

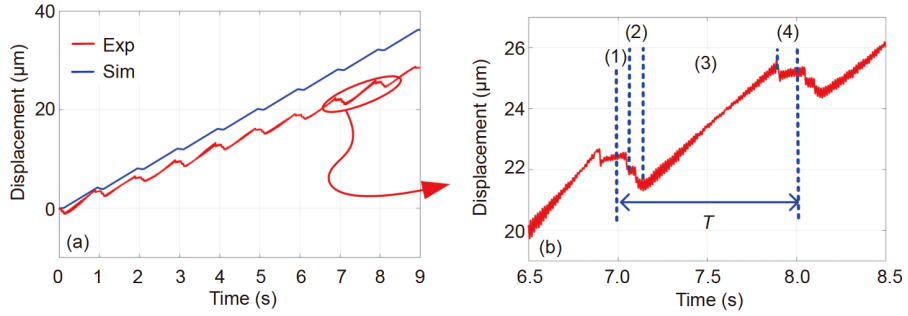

Figure 8 (Color online) The simulation and the experimental results in the inertial actuation mode. (a) The comparison results; (b) the enlargement of the experiment result using the longitudinal function module.

4.2 Open-loop experiment performance

Open-loop experiments are performed to investigate the output performances in the direct actuation mode and inertial actuation mode.

4.2.1 Direct actuation mode

The working range of the platform is measured through sinusoidal signals under different frequencies. The experimental results using the longitudinal function module (ULFM) and not using the longitudinal function module (NULFM) are measured, respectively, as shown in Figure 9, the amplitude of the voltage applied to PZT group-B is 600 $V_{p\text{-}p}$, those applied to the PZT group-L are 300 V and 0 V at the ULFM and NULFM conditions, respectively. It can be found that the longitudinal deformation of the function module can broaden the displacement output range at high frequency band, this is because it enhances the contact stiffness, the slippage at high frequency band can be suppressed. The frequency at which the gain is −3 dB is tested, and that of 308 Hz is obtained at the ULFM condition, while that is 76 Hz at the NULFM condition. The scan frequency is broadened by 305.3% through the utilization of the longitudinal deformation of the function module. Thus, the proposed platform can operate at a frequency up to 308 Hz in the direct actuation mode, in which the scanning range is about 3.368 μm×3.396 μm.

The hysteresis curves are plotted under different frequencies, as shown in Figure 10, the linearity errors are listed in Table 3. The total hysteresis effect composed of the hysteresis effect of the function modules and the friction hysteresis is smaller than that of platform actuated by

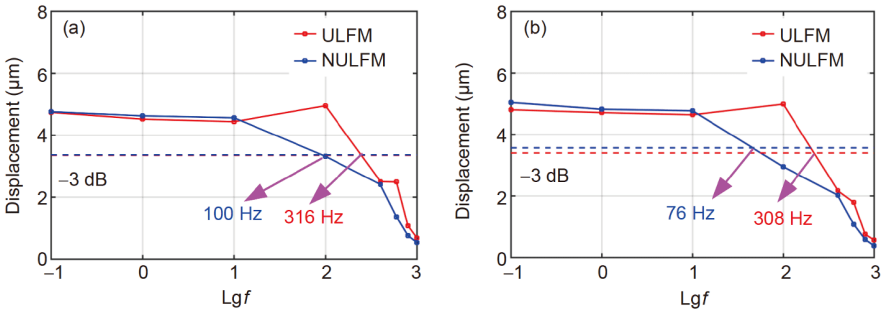

Figure 9 (Color online) Working range versus voltage (*f* is frequency). (a) Along axis *X*; (b) along axis *Y*.

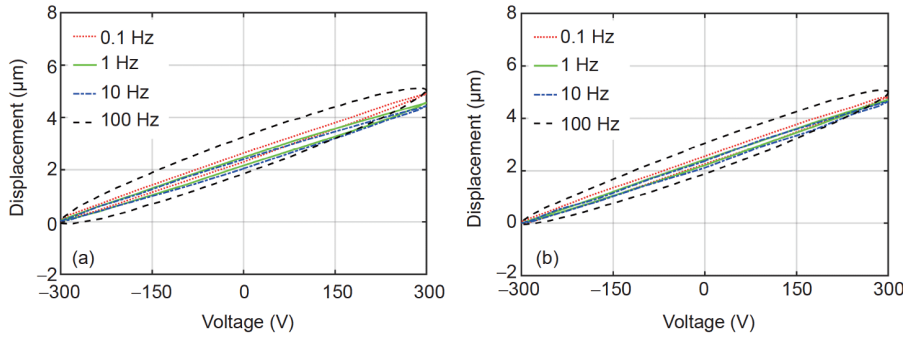

Figure 10 (Color online) Hysteresis loops of the platform at different frequencies. (a) Along axis *X*; (b) along axis *Y*.

Table 3 The linearity error along axes *X* and *Y* versus frequency

Frequency (Hz)	Linearity error along *X*	Linearity error along *Y*
0.1	7.22%	6.16%
1	7.04%	4.61%
10	8.65%	6.38%
100	28.61%	23.31%

commercial PZT stacks, for example, the linearity error of the platform proposed by Wu et al. is 9.32% at a frequency of 0.05 Hz and a voltage of 100 $V_{p\text{-}p}$ [38], while that of the proposed platform is 7.22% at a frequency of 0.1 Hz and a voltage of 600 $V_{p\text{-}p}$. This is because the connecting bolt is an elastic body with large rigidity, which can improve the rigidity of the actuator, causing a small hysteresis effect.

The stair step signal is used to test the displacement resolution along axis *X*, in which the frequency is 1 Hz, the voltages are from 210 to 224 V with interval of 2 V. The results are shown in Figure 11, the output displacement is about 16 nm under signal with an interval increment of 2 V. Thus, the output displacement resolution can be regarded as 16 nm in the direct actuation mode.

4.2.2 *Inertial actuation mode*

The response speed versus frequency is illustrated in Figure 12, where voltages applied to the PZT-X and PZT group-L are 600 $V_{p\text{-}p}$. The output speeds increase first and then decrease as the frequency increases, the reason for this phenomenon is that the response time for the function modules is about 1 ms, they cannot response to their full values, so the speeds fall down at high frequency. The maximum speeds occur at frequency of 800 Hz at the ULFM condition, those

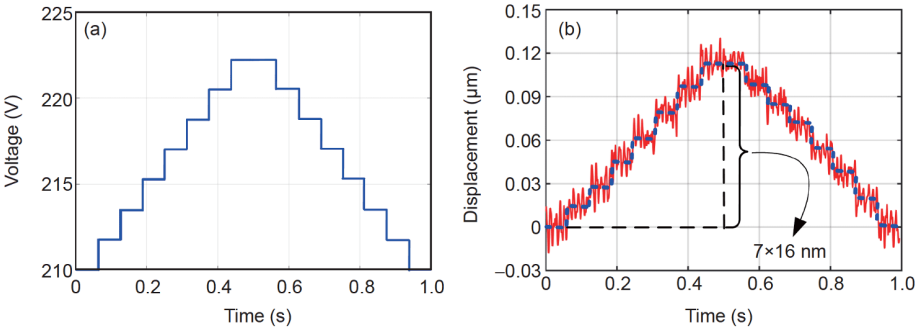

Figure 11 (Color online) Displacement resolution in direct actuation mode. (a) The stair step signal; (b) the experiment test displacement resolution.

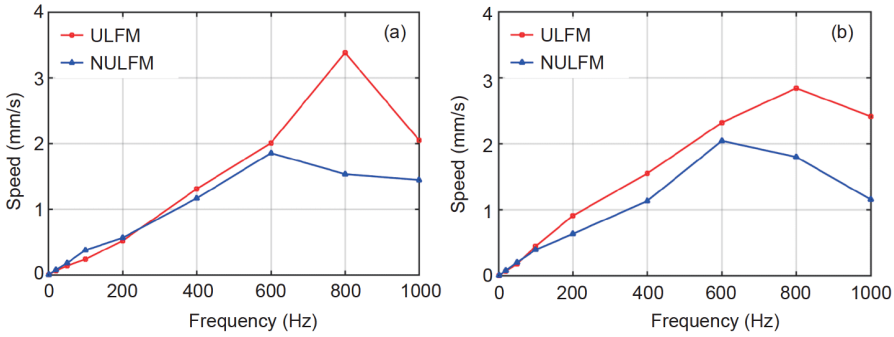

Figure 12 (Color online) Output speeds versus frequencies. (a) Along axis *X*; (b) along axis *Y*.

along axes *X* and *Y* are 3.38 and 2.84 mm s^{-1}, while those along axes *X* and *Y* are 1.86 and 2.04 mm s^{-1} at frequency of 600 Hz at the NULFM condition, the maximum speeds are increased by 81.7% and 39.2% through using the longitudinal function modules. Moreover, it can be found that the speeds are improved obviously by using the longitudinal function modules in frequency band higher than 100 Hz, especially in frequency band higher than 600 Hz, this is because the longitudinal deformation of the function modules can enhance the friction force in the stick step, there is smaller slippage in the stick step at high frequency according to the stick-slip mechanism, so the displacement distances at the ULFM condition are bigger than those at the NULFM condition in high frequency band. As a result, the proposed longitudinal deformation function modules can extend the displacement distances at high frequencies, thus increasing the output speeds of the piezoelectric platform.

4.3 Close-loop experiment performance

One of the main applications of the proposed platform is the high frequency scanning in large working range. The closed-loop experiments are carried out to obtain the switching of the inertial and direct actuation modes automatically, and to achieve the desired outputs. The control diagram of axis *X* is shown in Figure 13. There are two steps for the process, the details are as follows:

Step (1)-*positioning*: in switch position P_1, PID controller is adopted to achieve the point positioning, the platform operates at the inertial actuation mode with a large working range and reaches to the target position.

Step (2)-*scanning*: in switch position P_2, the platform performs high frequency scanning at the direct actuation mode in the open-loop condition, as the good output characteristics at high frequency, the switch condition is that the system runs for 1 s.

The target position is set as 10 μm in step (1), the switch from Steps 1 to 2 is performed when the system runs for 1 s, the frequency and voltage applied to the bending and longitudinal function modules are 600 $V_{p\text{-}p}$ and 800 Hz, while the

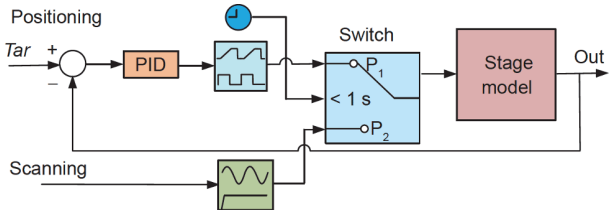

Figure 13 (Color online) Closed-loop control diagram of axis *X* of the platform. *Tar* is the position target value, *Out* is the output of the platform, the switch diagram defines which actuation modes is used: position P_1 for the inertial actuation mode, and position P_2 for the direct actuation mode.

voltages applied to the bending and longitudinal function modules in step (2) are 600 $V_{p\text{-}p}$ and 300 V, the scanning frequency are 10, 100 and 300 Hz, the experimental results are presented in Figure 14. The outputs keep steady at frequency up to 300 Hz in the scanning step, and the scanning stroke is about 3.369 μm at frequency of 300 Hz (Figure 14 (c) and (d)). As a conclusion, the proposed piezoelectric platform can achieve stable scanning at the frequency of 300 Hz in a large range at the set position under the proposed strategy.

The high-speed XYZ-nanopositioner proposed by Watanabe and Ando [16] can achieve high frequency scan with positioning precision better than 10 nm. The related characteristics are slightly better than those of the proposed platform with positioning precision better than 16 nm. But the travel range is 34 μm×34 μm×6 μm, which is far less than that of 15 mm×15 mm in this study. As a result, the proposed platform not only realizes nano-positioning and high frequency scanning, but also has large travel range compared with the previous designs.

5 Conclusion

A piezoelectric nano-positioning platform based on function module actuator was developed and tested. The direct and inertial combining actuation modes were accomplished by flexibly combing the function modules of the piezoelectric

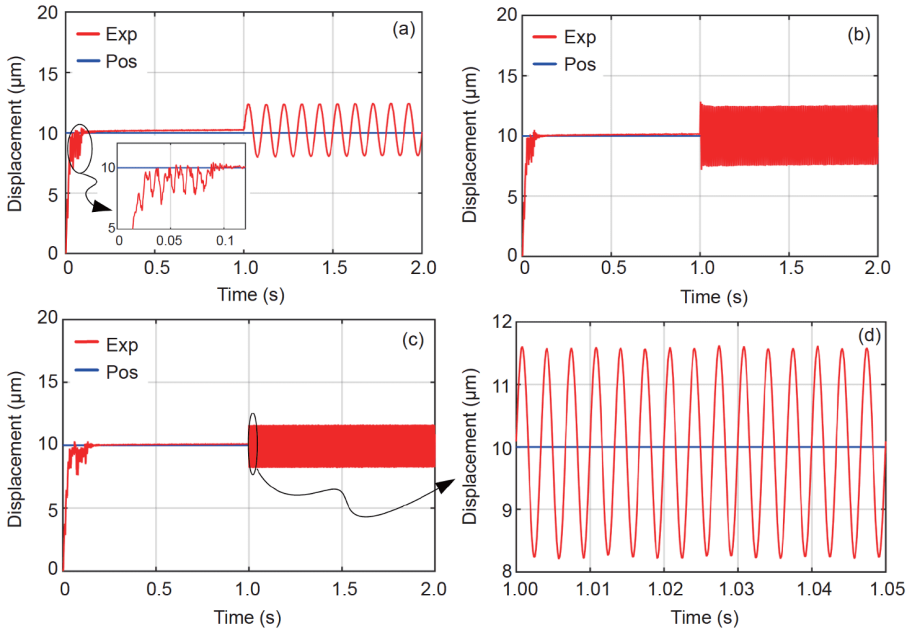

Figure 14 (Color online) Experimental controlled position of axis *X*. (a) At 10 Hz; (b) at 100 Hz; (c) at 300 Hz; (d) enlarge of (c).

actuator. A dynamic model was established, which could be used for not only the structural design and optimization, but also the excitation scheme planning. The experiment results showed that the proposed function module actuator had small hysteresis, when operating in the direct actuation mode, the longitudinal deformation of the function modules broadened the scan frequency by 305.3%, the platform could operate at high scan rate up to 308 Hz with range of 3.368 μm×3.396 μm. The maximum speeds of 3.38 and 2.84 mm s^{-1} were achieved in the inertial actuation mode, the maximum speeds were increased by 81.7% and 39.2% as that the rollback problem of the platform was alleviated through the longitudinal deformation. Besides, the platform obtained the switching of the inertial and direct actuation modes automatically through closed-loop control, and it could achieve stable scanning at a frequency of 300 Hz at the set position. The multi-actuation modes of the platform can be used to meet different output requirements through the flexible combination of the proposed function module actuator.

This work was supported by the National Natural Science Foundation of China (Grant Nos. U1913215 & 51975162).

1 Lu H, Shang W, Xie H, et al. Ultrahigh-precision rotational positioning under a microscope: Nanorobotic system, modeling, control, and applications. IEEE Trans Robot, 2018, 34: 497–507
2 Zhu W L, Zhu Z, He Y, et al. Development of a novel 2-D vibration-assisted compliant cutting system for surface texturing. IEEE/ASME Trans Mechatron, 2017, 22: 1796–1806
3 Lee C, Salapaka S M. Model based control of dynamic atomic force microscope. Rev Sci Instrum, 2015, 86: 043703
4 Li L L, Li C X, Gu G, et al. Modified repetitive control based cross-coupling compensation approach for the piezoelectric tube scanner of atomic force microscopes. IEEE/ASME Trans Mechatron, 2019, 24: 666–676
5 Salim M, Salim D, Chandran D, et al. Review of nano piezoelectric devices in biomedicine applications. J Intel Mat Syst Str, 2018, 29: 2105–2121
6 Wei Y Z, Xu Q S. A survey of force-assisted robotic cell micro-injection technologies. IEEE Trans Automat Sci Eng, 2019, 16: 931–945
7 Xu D M, Liu Y X, Shi S J, et al. Development of a non-resonant piezoelectric motor with nanometer resolution driving ability. IEEE/ASME Trans Mechatron, 2018, 23: 444–451
8 Yokozawa H, Doshida Y, Kishimoto S, et al. Resonant-type smooth impact drive mechanism actuator using lead-free piezoelectric material. Sens Actuat A-Phys, 2018, 274: 179–183
9 Liu J, Liu Y, Zhao L, et al. esign and experiments of a single-foot linear piezoelectric actuator operated in stepping mode. IEEE Trans Ind Electron, 2018, 65: 8063–8071
10 Liu Y, Yan J, Wang L, et al. A two-DOF ultrasonic motor using a longitudinal-bending hybrid sandwich transducer. IEEE Trans Ind Electron, 2019, 66: 3041–3050
11 Lai L J, Gu G Y, Zhu L M. Design and control of a decoupled two degree of freedom translational parallel micro-positioning stage. Rev Sci Instrum, 2012, 83: 045105
12 Schitter G, Stemmer A. Identification and open-loop tracking control of a piezoelectric tube scanner for high-speed scanning-probe microscopy. IEEE Trans Contr Syst Technol, 2004, 12: 449–454
13 Yong Y K, Moheimani S O R, Kenton B J, et al. Invited review article: High-speed flexure-guided nanopositioning: Mechanical design and control issues. Rev Sci Instrum, 2012, 83: 121101
14 Li C X, Gu G Y, Yang M J, et al. Design and analysis of a high-speed XYZ nanopositioning stage. In: 2015 International Conference on Manipulation, Manufacturing and Measurement on the Nanoscale (3M-NANO). Changchun, 2015. 229–234
15 Yong Y K, Bhikkaji B, Reza Moheimani S O R. Design, modeling, and fpaa-based control of a high-speed atomic force microscope nanopositioner. IEEE/ASME Trans Mechatron, 2013, 18: 1060–1071
16 Watanabe S, Ando T. High-speed XYZ-nanopositioner for scanning ion conductance microscopy. Appl Phys Lett, 2017, 111: 113106
17 Qin Y, Tian Y, Zhang D, et al. A novel direct inverse modeling

approach for hysteresis compensation of piezoelectric actuator in feedforward applications. IEEE/ASME Trans Mechatron, 2013, 18: 981–989
18 Wei Y J, Wu C D. Modeling of nano piezoelectric actuator based on block matching algorithm with optimal block size. Sci China Tech Sci, 2013, 56: 2649–2657
19 Gu G Y, Zhu L M, Su C Y, et al. Modeling and control of piezo-actuated nanopositioning stages: A survey. IEEE Trans Automat Sci Eng, 2016, 13: 313–332
20 Gu G Y, Li C X, Zhu L M, et al. Modeling and identification of piezoelectric-actuated stages cascading hysteresis nonlinearity with linear dynamics. IEEE/ASME Trans Mechatron, 2016, 21: 1792–1797
21 Liang C, Wang F, Tian Y, et al. Grasping force hysteresis compensation of a piezoelectric-actuated wire clamp with a modified inverse Prandtl-Ishlinskii model. Rev Sci Instrum, 2017, 88: 115101
22 Wang R, Zhang X. A planar 3-DOF nanopositioning platform with large magnification. Precision Eng, 2016, 46: 221–231
23 Zhang X, Zhang Y, Xu Q. Design and control of a novel piezo-driven XY parallel nanopositioning stage. Microsyst Technol, 2017, 23: 1067–1080
24 Shi S J, Liu J K, Chen W S et al. Development of a 2-DOF planar ultrasonic motor using longitudinal-bending hybrid transducer. In: 2009 18th IEEE International Symposium on the Applications of Ferroelectrics. Xi'an, 2009. 341–345
25 Merry R J E, Maassen M G J M, van de Molengraft M J G, et al. Modeling and waveform optimization of a nano-motion piezo stage. IEEE/ASME Trans Mechatron, 2011, 16: 615–626
26 Rong W, Liang S, Wang L, et al. Model and control of a compact long-travel accurate-manipulation platform. IEEE/ASME Trans Mechatron, 2017, 22: 402–411
27 Xu D M, Liu Y K, Liu J K, et al. Developments of a piezoelectric actuator with nano-positioning ability operated in bending modes. Ceramics Int, 2017, 43: S21–S26
28 Deng J, Liu Y K, Liu J K, et al. Development of a planar piezoelectric actuator using bending-bending hybrid transducers. IEEE Trans Ind Electron, 2019, 66: 6141–6149
29 Chen Z, Li X, Liu G, et al. A two degrees-of-freedom piezoelectric single-crystal micromotor. J Appl Phys, 2014, 116: 224101
30 Liu Y, Wang L, Gu Z, et al. Development of a two-dimensional linear piezoelectric stepping platform using longitudinal bending hybrid actuators. IEEE Trans Ind Electron, 2019, 66: 3030–3040
31 Li J P, Zhou X Q, Zhao H W, et al. Development of a novel parasitic-type piezoelectric actuator. IEEE/ASME Trans Mechatron, 2017, 22: 541–550
32 Boudaoud M, Lu T, Liang S, et al. A voltage/frequency modeling for a multi-dofs serial nanorobotic system based on piezoelectric inertial actuators. IEEE/ASME Trans Mechatron, 2018, 23: 2814–2824
33 Oubellil R, Voda A, Boudaoud M, et al. Mixed stepping/scanning mode control of stick-slip sem-integrated nano-robotic systems. Sens Actuat A-Phys, 2019, 285: 258–268
34 Hutchinson J R. Shear coefficients for Timoshenko beam theory. J Appl Mech, 2001, 68: 87–92
35 Deng J, Liu Y X, Chen W S, et al. A XY transporting and nanopositioning piezoelectric robot operated by leg rowing mechanism. IEEE/ASME Trans Mechatron, 2019, 24: 207–217
36 Brown S R, Scholz C H. Closure of random elastic surfaces in contact. J Geophys Res, 1985, 90: 5531–5545
37 Wit C C, Olsson H, Astrom K J, et al. A new model for control of systems with friction. IEEE Trans Automat Contr, 1995, 40: 419–425
38 Wu Z Y, Xu Q S. Design, fabrication, and testing of a new compact piezo-driven flexure stage for vertical micro/nanopositioning. IEEE Trans Automat Sci Eng, 2019, 16: 908–918